ACS Photonics

pubs.acs.org/journal/apchd5

Article

Robustness Analysis of Metasurfaces: Perfect Structures Are Not Always the Best

Hsiang-Chu Wang, Karim Achouri, and Olivier J. F. Martin*

Cite This: ACS Photonics 2022, 9, 2438−2447

Read Online

ACCESS | Metrics & More | Article Recommendations | Supporting Information

Downloaded via ECOLE POLYTECHNIC FED LAUSANNE on August 19, 2022 at 06:21:54 (UTC).
See https://pubs.acs.org/sharingguidelines for options on how to legitimately share published articles.

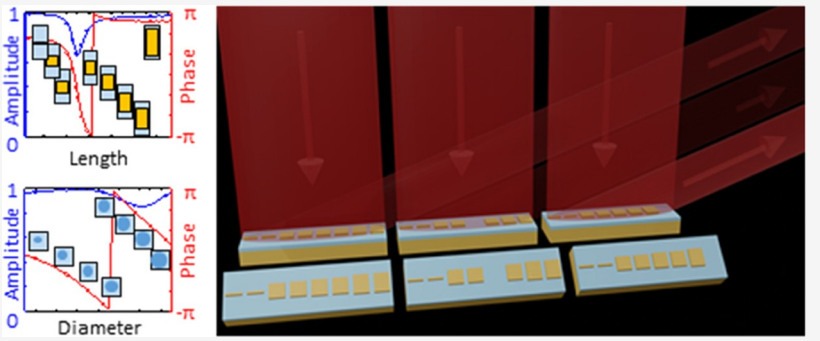

ABSTRACT: Optical metasurfaces rely on subwavelength scale nanostructures, which puts significant constraints on nanofabrication accuracies. These constraints are becoming increasingly important, as metasurfaces are maturing toward real applications that require the fabrication of very large area samples. Here, we focus on beam steering gradient metasurfaces and show that perfect nanofabrication does not necessarily equate with best performances: metasurfaces with missing elements can actually be more efficient than intact metasurfaces. Both plasmonic metasurfaces in reflection and dielectric metasurfaces in transmission are investigated. These findings are substantiated by experiments on purposely misfabricated metasurfaces and full-wave calculations. A very efficient quasi-analytical model is also introduced for the design and simulations of metasurfaces; it agrees very well with full-wave calculations. Our findings indicate that the substrate properties play a key role in the robustness of a metasurface and the smoothness of the approximated phase gradient controls the device efficiency.

KEYWORDS: *metasurfaces, beam steering, imperfection, plasmonics, dielectric, efficiency*

INTRODUCTION

Already at the turn of the 21st century, it was recognized that metallic nanostructures organized on a surface could mold the flow of light by manipulating its phase.[1] A few years later, this field of research developed vividly into that of optical metasurfaces: first at microwave and radio frequencies,[2−4] later in the infrared,[5−11] and finally, in the visible part of the optical spectrum.[12−16] This spectral evolution was made possible by tremendous progress in nanofabrication since the dimensions of the structures building the device, the so-called meta-atoms, must be smaller than the operation wavelength to produce a homogeneous response.[17,18]

Significant efforts have been devoted to the development of precise nanofabrication techniques for metasurfaces.[19−21] In most cases, the meta-atoms are defined using electron-beam (E-beam) lithography;[22−30] sometimes ultraviolet photolithography is used,[31−34] or they are directly carved using focused ion beams.[35−37] Meta-atoms are fabricated in either dielectrics[16,38,39] or plasmonic metals.[40,41] The latter has an especially important interaction with light, due to the excitation of free electron resonances.[42] After the exposure step, the meta-atoms are created either by lift-off or by etching.[43] Irrespective of the approach, nanofabrication is definitely a rather challenging activity, often with a relatively low yield. Over an entire wafer, it is difficult to fabricate structures that are as perfect as the original design. The size of the meta-atoms can vary with the lithography dose; some nanostructures may be deformed during the lithography by proximity effects associated with neighboring nanostructures.[44] The adhesion of some meta-atoms can be poor, such that they disappear during the process; this is especially the case for metal nanostructures on dielectric substrates.[45−47] The metal evaporation can produce nanostructures with slanted sides as the photoresist is clogged up during deposition.[48]

Received: April 13, 2022
Published: June 28, 2022

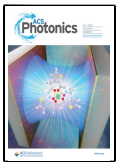

© 2022 The Authors. Published by American Chemical Society

The aim of this paper is to study the influence of such inaccuracies in nanofabrication on the overall response of metasurfaces, especially the tolerance of nanofabrication that is acceptable without corrupting the optical response excessively. Both a quasi-analytical model and full-wave electromagnetic simulations are used to determine the influence of such fabrication misshapes. In addition, purposely misfabricated samples are studied experimentally to gain insights into the mechanisms that control the performance of metasurfaces. Although the present study focuses on beam steering gradient plasmonic metasurfaces using gap plasmon meta-atoms,[49−51] the findings reported therein can also be applied to other metasurface designs and materials,[52−54] since the nanofabrication techniques are very similar.

RESULTS AND DISCUSSION

The metasurface considered here is based on gold nanostructures of varying dimensions deposited above a gold mirror using a SiO_2 spacer (Figure 1). This reflecting substrate

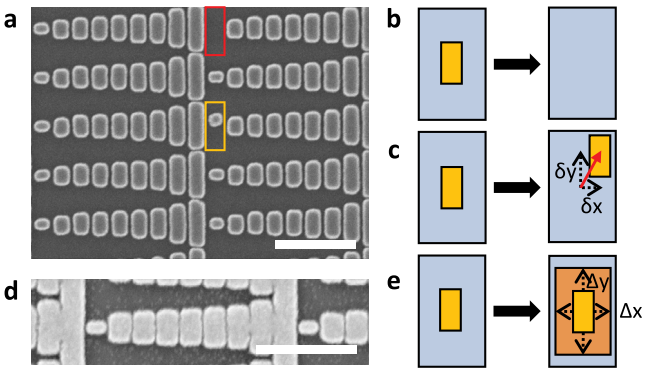

Figure 1. Examples of possible imperfections that can occur during the nanofabrication of an eight-level metasurface: (a) scanning electron microscopy (SEM) image of an area of the metasurface with defects such as (b) missing element or (c) displaced element. (d) SEM image of an overexposed metasurface, with oversized elements (e) (Scale bars: 500 nm).

provides an additional phase to the scattered light, such that a full 2π phase range can be engineered for the metasurface response.[55] The metasurface is fabricated using E-beam lithography and ion beam etching, as described in the Methods section. In spite of a careful nanofabrication procedure, including dose tests for the electron-beam lithography and optimized etching time, it is almost impossible to avoid imperfections in the fabricated metasurface, especially over the relatively large area (typically tens of μm^2) required to implement a meaningful optical function. Misfabrication leads to defects such as missing elements (Figure 1a,b), displaced elements (Figure 1a,c), or bloated elements (Figure 1d,e). The aim of this paper is to study theoretically and experimentally the influence of such defective elements on the overall metasurface response.

The metasurface unit cell is illustrated in Figure 2: h = 30-nm-thick Au nanostructures (meta-atoms) with a width w = 140 nm and different lengths L are deposited atop a gold mirror (thickness 150 nm, such that the mirror can be considered as semi-infinite) with a t = 40 nm SiO_2 spacer (Figure 2a). The system builds unit cells with dimensions P_x = 180 nm and P_y = 430 nm in x- and y-directions, respectively.

Changing the nanostructure length L controls the phase of the reflected light for illumination with y-polarized light, as shown in Figure 2b for the operation wavelength λ = 980 nm. These data were obtained using full-wave simulations, as described in the Methods section. Varying the nanostructure length L between 0 and 400 nm changes the phase of the reflected light over a 2π range while maintaining the amplitude of the reflection coefficient relatively constant around unity, except for L = 150 nm, where the excitation of a localized resonance increases absorption and reduces reflectance. To analyze missing meta-atoms, we replace the missing element with a bare substrate, i.e., with its corresponding amplitude (0.99) and phase (107°) of the reflection coefficient, computed at the same height as the other elements.

The deflection angle θ for a beam steering device under normal incidence illumination is defined as $\theta = \sin^{-1}(\lambda/\Lambda)$, where λ is the working wavelength and Λ is the superlattice period, which is $\Lambda = nP_x$, where n represents the number of discretized elements used for the metasurface, which is eight in this work. Two different designs can achieve the same beam steering functionality: an eight-level design, which maximizes the phase discretization levels and has a smoother phase gradient (Figure 2c), or a four-level design, with a coarser phase discretization (Figure 2d). Both designs have been reported in the literature.[4,12,13] Since they have the same superlattice period Λ, they deflect light in the same direction $\theta \simeq 43°(\lambda = 980\ nm)$ and their robustness and performance can be compared in the following.

A simple quasi-analytical model is derived in the Methods section to compute the momentum provided by the metasurface upon reflection. Based on Fourier transforms, this model is extremely efficient for computing the metasurface response and can be used to evaluate its performance. In short, the superlattice period is replaced by a collection of discrete points, each representing one meta-atom by its reflection amplitude and phase, as illustrated at the bottom of Figure 2c,d. These amplitude and phase values were obtained from full-wave simulations, as described in the Methods section. With this approach, it is also very simple to compute the response of a metasurface with one or several missing meta-atoms, which are then replaced by the amplitude and phase of the substrate reflection.

Let us first use this model to study in Figure 3 the performance of eight-level metasurfaces with different missing elements. We label the intact structure as Sample #0 and a metasurface where the meta-atom m is missing as Sample #m. For a perfect eight-level device, the efficiency is 0.66, meaning that 66% of the incoming energy is redirected into the diffraction order at an angle θ (see Sample #0 in Figure 3a). The remaining energy is absorbed in and scattered by the device. When one element is missing, light is still redirected into the direction θ, but part of the energy is also specularly reflected and absorbed, making the device less efficient (see for example Sample #5 in Figure 3a), which has only an efficiency of 37%. Surprisingly, each meta-atom does not have the same influence on the performance, as summarized in Figure 3c: counterintuitively, it is not when the largest elements #7 and #8 are removed that the efficiency deteriorates most but rather missing elements around #5 appear especially detrimental to the metasurface performance. On the other hand, when the first meta-atom is missing (Sample #1), the performance is the same as the complete structure (Sample #0), because both the substrate and the first meta-atom (L = 20 nm) produce the

https://doi.org/10.1021/acsphotonics.2c00563
ACS Photonics 2022, 9, 2438−2447

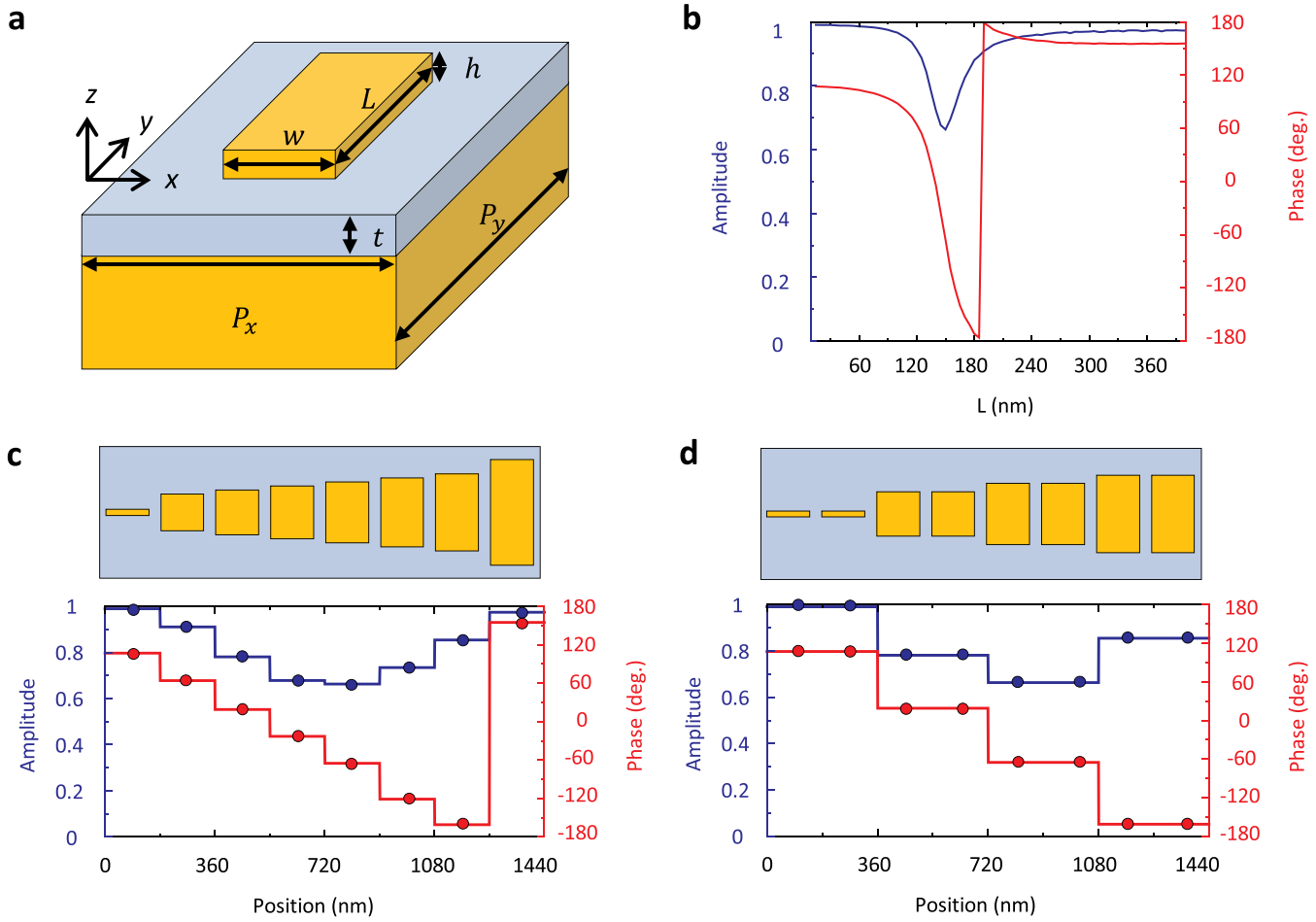

Figure 2. (a) Schematic of the metallic meta-atom and (b) corresponding amplitude and phase of the reflection coefficient as a function of the length L of the gold nanorod at λ = 980 nm. Two common configurations to achieve beam steering with a phase gradient metasurface covering a full 2π range for the phase modulation with an (c) eight-level unit cell with meta-atoms of lengths L = 20, 120, 135, 143, 150, 160, 175, and 345 nm and a (d) four-level unit cell with meta-atoms of lengths L = 20, 135, 150, and 175 nm (each element being repeated). The discrete elements used for the corresponding simplified model are shown beneath panels (c, d).

same amplitude and phase for the reflected field (see Figure 2b).

The special role of element #5 is also observed for a four-level device, as indicated in Figure 3c. Those devices have somewhat lower performance than the eight-level devices, with an efficiency of only 56% for the perfect metasurface due to the coarser phase gradient. However, the decrease in performance caused by element #5 missing is similar for eight- and four-level devices. On the other hand, the scattering direction θ is maintained for both devices, even when a meta-atom is missing.

Figure 3c also provides the efficiency for the defective devices computed with full-wave simulations (see the Methods section). The agreement between those simulations and the simple model is very good and we also recover with full-wave simulations the strong influence of element #5. The small differences between the full-wave simulations and the model stem from the fact that the latter does not include the near-field interactions between neighboring elements. The efficiency computed with full-wave simulations for the four-level device is quite surprising: sample #8, with a missing element, has a higher efficiency (56%) than the perfect one (52%), and only sample #5 drops noticeably in performance (31%) (see the purple diamonds in Figure 3c). To gain insights into the underlying mechanisms, Figure 3b shows the amplitude of the total electric field for Samples #1 (left part) and #5 (right part). Surprisingly, it is very difficult to distinguish in the electric field distribution any difference between both devices.

To investigate this further, we have fabricated samples for both eight-level (Figure 4a) and four-level devices (Figure 4b). Purposely misfabricated samples with missing specific elements were realized, as described in the Methods section and in the Supporting Information (Figure S1). The left parts of Figure 4a,b illustrate the large area samples that were produced; this was also the case for the misfabricated metasurfaces, of which only excerpts are shown in the right parts. Complete misfabricated metasurfaces are shown in the Supporting Information, Figure S2 for eight-level devices and in the Supporting Information, Figure S3 for four-level devices. The optical response of these different metasurfaces was measured using an optical microscope as detailed in the Methods section and in the Supporting Information, Figure S4. Figure 4c shows the measured intensity profiles for both devices (purple lines for the four-level devices and green lines for the eight-level devices). For each device, the efficiency is computed as the power integrated over the entire deflected beam with its center at the angle $\theta \simeq 43°$, divided by the measured power reflected by a mirror that replaces the sample. The corresponding values

https://doi.org/10.1021/acsphotonics.2c00563
ACS Photonics 2022, 9, 2438−2447

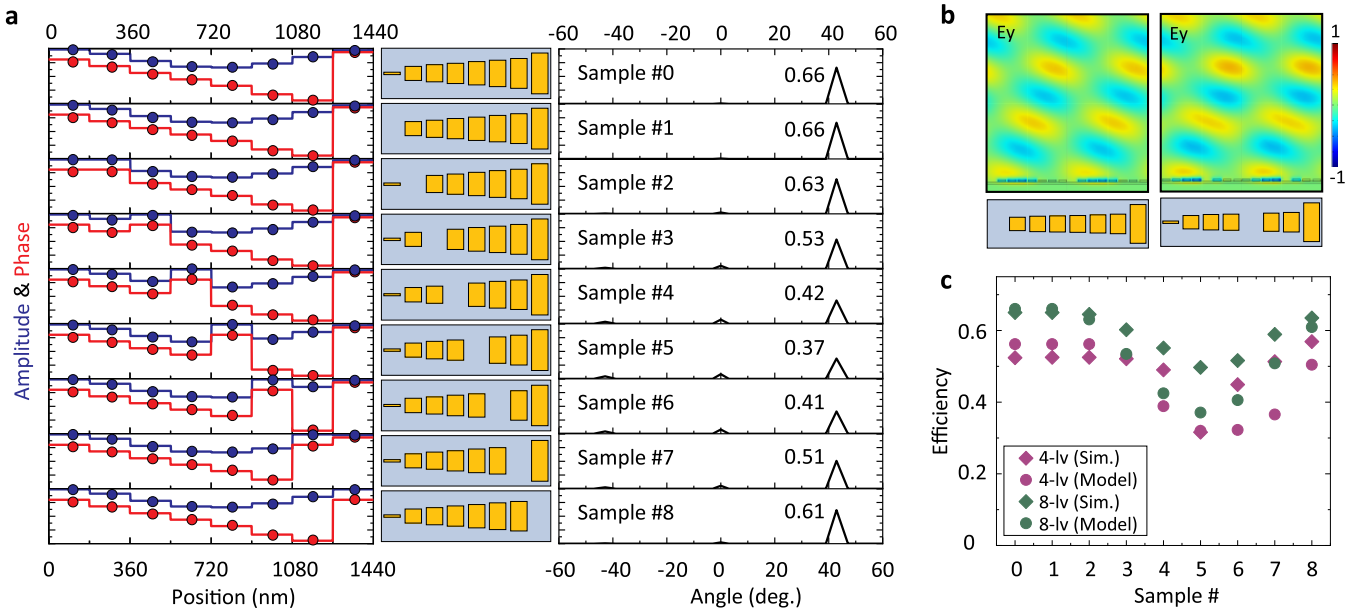

Figure 3. Performance of metasurfaces with a missing element. (a) Phase and amplitude of the reflection coefficient used for each element in the simplified model (left panel), schematics of the corresponding unit cell (middle panel), and angular response obtained with the simple model (right panel). (b) Full-wave calculations of the total (incident + reflected) electric field E_y component amplitude distribution for sample #1 (left panel) or sample #5 (right panel). (c) Metasurface performance as a function of the sample number for eight-level and four-level metasurfaces, computed using full-wave simulations or the simplified model.

are reported in Figure 4d, where the error bars correspond to a series of measurements with different measurement areas, as described in the Methods section and in the Supporting Information, Figure S4. According to the experimental results, for the eight-level device (green squares), as expected, Sample #1 has almost the same performance as the perfect sample (sample #0). Surprisingly, Samples #2 and #3 have higher performance than the perfect one, while the others follow a similar trend as the semianalytical model and the full-wave simulations with Sample #5 exhibiting the lowest performance. For the four-level devices (purple squares in Figure 4d), as expected from the calculations, sample #8 has an outstanding performance, while Samples #3 and #4 perform also better than the perfect one (Sample #0). In addition to Sample #5, Sample #7 also has the lowest efficiency.

Next, we elucidate why the fifth element has such a significant influence on the metasurface performance: when it is missing and replaced by a highly reflective substrate, the efficiency decreases most. After investigating different parameters, we came to the conclusion that this behavior is related to the phase provided by the substrate upon reflection. In Figure 5a, we take the same configuration of an eight-level device as in Figure 2c, but this time we keep the reflection amplitude of each meta-atom as unity while keeping the phase gradient values as derived from full-wave simulations such that we can clearly see how the phase of the substrate directly affects the device performance. We compute again with the simple model the device efficiency when one meta-atom is missing (Samples #0 ... #8). In addition, we modify the phase associated with the substrate reflection φ_{sub}, increasing it gradually from 0 to 315° (Figure 5b). First, we notice that for the same substrate as used previously, with a reflection phase of 107°, we recover the results obtained in Figure 3c with the strong efficiency loss for Sample #5, in spite of keeping the reflection amplitude constant. When we change the substrate reflection phase, we observe in Figure 5b that different elements dominate the metasurface efficiency. For example, it is element #7 that dominates the efficiency when the substrate reflection phase is 0°. From the data in Figure 5b, we can conclude that the lowest efficiency occurs when the element with the largest phase difference from the substrate is removed (180° in this case). From an experimental point of view, let us note that the phase produced by the substrate strongly depends on the dielectric spacing layer.[55]

A similar analysis is performed in the Supporting Information, Figure S5 for four-level devices. In this case, we observe that the overall device efficiencies are lower than their eight-level counterparts. Even for the ideal case used in the simplified model, where each element reflects an amplitude equal to 1, the performance is only 83% due to the coarser phase gradient (it reaches 97% for the eight-level devices, Figure 5). The surprising fact that a metasurface with missing elements can perform as well or even better than a complete metasurface is easily understood by the fact that it approximates the phase gradient better. For example, if we consider the phase substrate φ_{sub} = 0 and remove the meta-atom #4, which provides the best performance in the Supporting Information, Figure S5a, the corresponding phase distribution, shown in the Supporting Information, Figure S5b, is very smooth. Since in a four-level metasurface, both meta-atoms #3 and #4 produce the same phase, one could think that having either of them missing would deteriorate the performance in a similar fashion. Supporting Information, Figure S5c indicates that this is not the case and, from the previous discussion, we have learned that the origin is the worse phase discretization when #3 is replaced by the substrate. Note that one could make good use of these observations to optimize device performances.

Let us now resort to full-wave simulations to study other imperfections such as displaced or bloated nanostructures. In Figure 6, the performance of the eight-level device is not significantly affected by the displacement of a single

https://doi.org/10.1021/acsphotonics.2c00563
ACS Photonics 2022, 9, 2438−2447

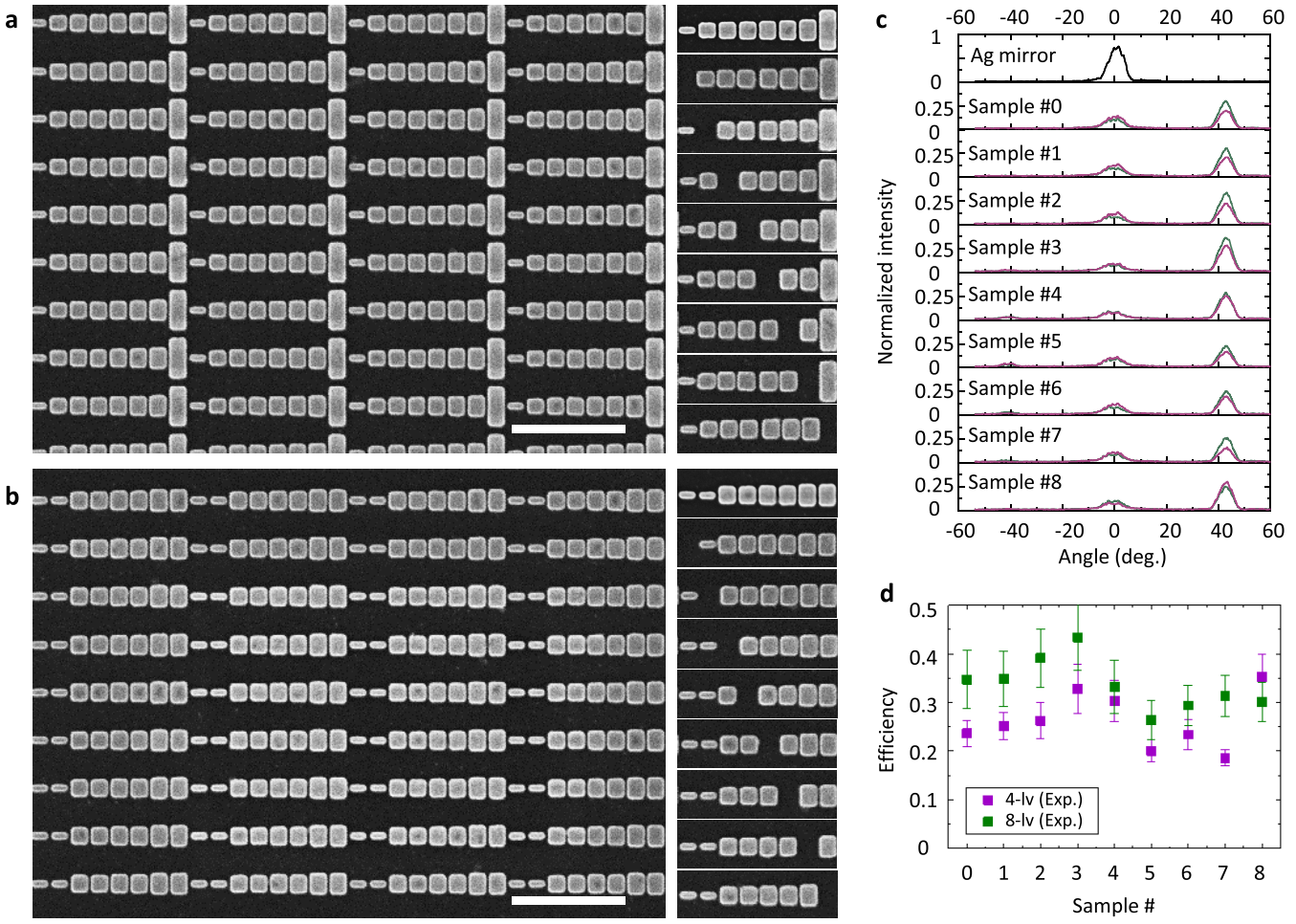

Figure 4. Experimental results for eight-level and four-level devices. Fabricated samples (a) for the eight-level devices and (b) for the four-level devices. The images on the left show part of the perfect Sample #0 (scale bars: 1 μm), while the images on the right show excerpts taken out of the misfabricated samples (the complete misfabricated samples are shown in the Supporting Information, Figures S2 and S3). (c) Intensity profiles were measured in the Fourier plane (green for the eight-level devices and purple for the four-level devices). (d) Measured efficiency for each device at the deflection angle $\theta \simeq 43°$ (see the text for details).

nanostructure in *x*-, *y*-, or *xy*-directions. Maximum possible displacements are δx = 35 nm and δy = 30 nm (for larger δy, the largest meta-atom would overflow the unit cell). Since the spacing along *x*-direction between two adjacent nanorods is only 40 nm in the original design, a δx = 35 nm displacement for one nanostructure leaves only 5 nm between neighboring nanostructures. Surprisingly, those displacements barely influence the overall device performance. This observation holds for displacements along both directions, as well as in the diagonal. Overall, the exact nanostructure alignment is not required for the device performance; it does not influence the steering angle θ either.

We also study in Figure 7 the influence of the meta-atoms size on the metasurface performance for an eight-level device. Structures that are larger or smaller than the original design are usually the result of an over- or under-exposed lithographic process and all structures will be affected in a similar way. Hence, we consider here that all of the eight structures that build the metasurface superlattice are modified in a similar amount in either *x*-, *y*-, or *xy*-directions. Both a positive (enlarged nanostructures) and a negative (shrunk nanostructures) variation Δ is considered. We observe in Figure 7 that size variations in *x*-direction do not influence much the device performance, since the light of interest is polarized in the *y*-direction. On the other hand, over- or under-sized nanostructures in the *y*-direction deteriorate the device performance since a change in the nanostructure length *L* modifies the amplitude and phase of the reflected light (Figure 2b). This effect is however quite marginal for variations between Δy = −10 nm and Δy = 5 nm, leading to a maximal efficiency reduction of only 5%. For larger variations, the performance begins to be affected significantly, for example, for Δy = 20 nm, the efficiency drops to half that of the perfect one, although the steering angle θ is not affected by all of these changes.

Let us now briefly investigate another type of device: dielectric metasurfaces that operate in transmission. The meta-atoms are TiO_2 cylinders with a fixed height *H* = 600 nm and varying diameters *D* (Figure 8a). Changing *D* tunes the phase shift of the transmitted light over 2π while keeping the transmission amplitude constant (Figure 8b). Similar to the metallic metasurface, we investigate both eight-level and four-level devices (Figure 8c,d) and study with full-wave calculations the response of imperfect metasurfaces with a missing element #m. The efficiency as a function of the sample number is summarized in Figure 8e. For the eight-level dielectric devices, sample #8 has about the same performance (79%) as sample #0 (the complete device). For sample #2, the efficiency drops to only 63%. Surprisingly, sample #8 for the

https://doi.org/10.1021/acsphotonics.2c00563
ACS Photonics 2022, 9, 2438−2447

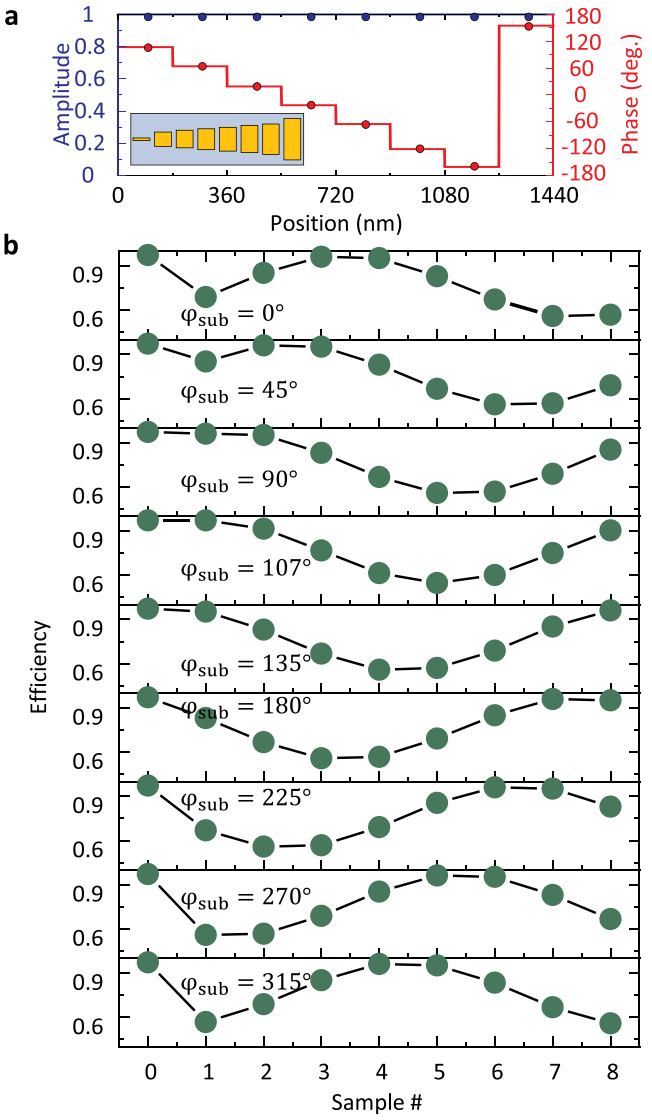

Figure 5. Efficiency of an artificial eight-level device calculated with the simple model, neglecting the variations of amplitude. (a) Phase values from previous full-wave simulations and the artificial unit amplitudes used. (b) Metasurface performance as a function of the sample number, i.e., of the missing element for nine substrates with different reflection phases indicated in the inset. The efficiency minimum occurs when the phase difference between the missing element and the substrate is 180°.

four-level dielectric device has the highest performance (83%), which is 18% higher than the perfect sample #0 (65%).

It is very surprising that some imperfect metasurfaces, both dielectric and metallic, can outperform perfect devices. To shed some light on this phenomenon, we use full-wave electromagnetic simulations in the Supporting Information, Figure S6 to compute the field distribution for perfect and imperfect dielectric devices. Four-level metasurfaces are chosen because sample #8 outperforms the ideal structure most for those devices. By comparing the different phase distributions, we observe that sample #8 exhibits a smoother phase gradient, compared to sample #0. On the other hand, sample #5, which has the worst efficiency, produces a very rough phase distribution (Supporting Information, Figure S6b). Consequently, although sample #8 is imperfect, its steady-state

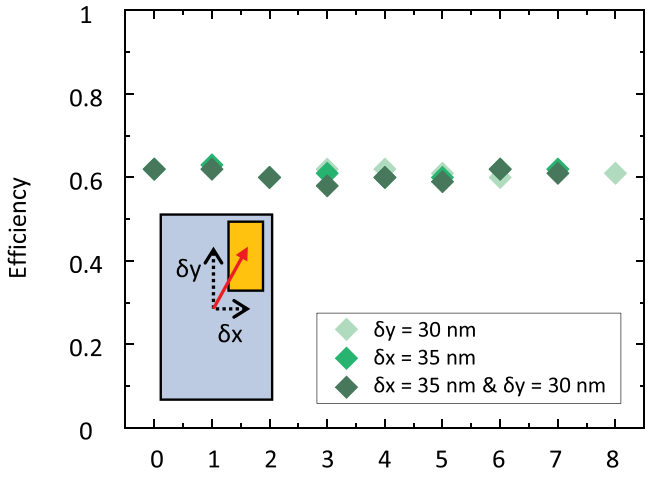

Figure 6. Performance computed for an eight-level metasurface with one element displaced along one direction (δx or δy) or along both directions.

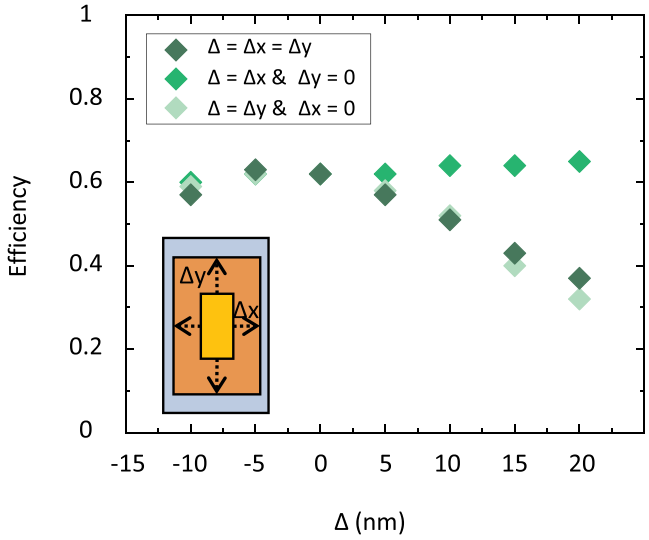

Figure 7. Performance plot for an eight-level metasurface as a function of the size change for all of the meta-atoms.

electric field distribution has a better fitting with the designed phase gradient and gives rise to a higher efficiency.

CONCLUSIONS

In summary, we have analyzed theoretically and experimentally the robustness of phase gradient metasurfaces to fabrication inaccuracies, considering both metallic devices in reflection and dielectric devices in transmission. To this end, a simple semianalytical model has been developed, which provides the response of a metasurface at almost no numerical costs and is in very good agreement with full-wave numerical simulations. This simple model could be used to design more complex metasurfaces, such as meta-holograms, for example.

Missing meta-atoms are the defects that deteriorate most of the device efficiency, reducing it typically by 20%. In that context, and quite surprisingly, it is not the meta-atom size that matters most, but rather its associated phase, with respect to the phase provided by the substrate. Elements that have the largest phase difference with the substrate (e.g., in the order of 180°) are the most sensitive ones. Consequently, by modifying

https://doi.org/10.1021/acsphotonics.2c00563
ACS Photonics 2022, 9, 2438−2447

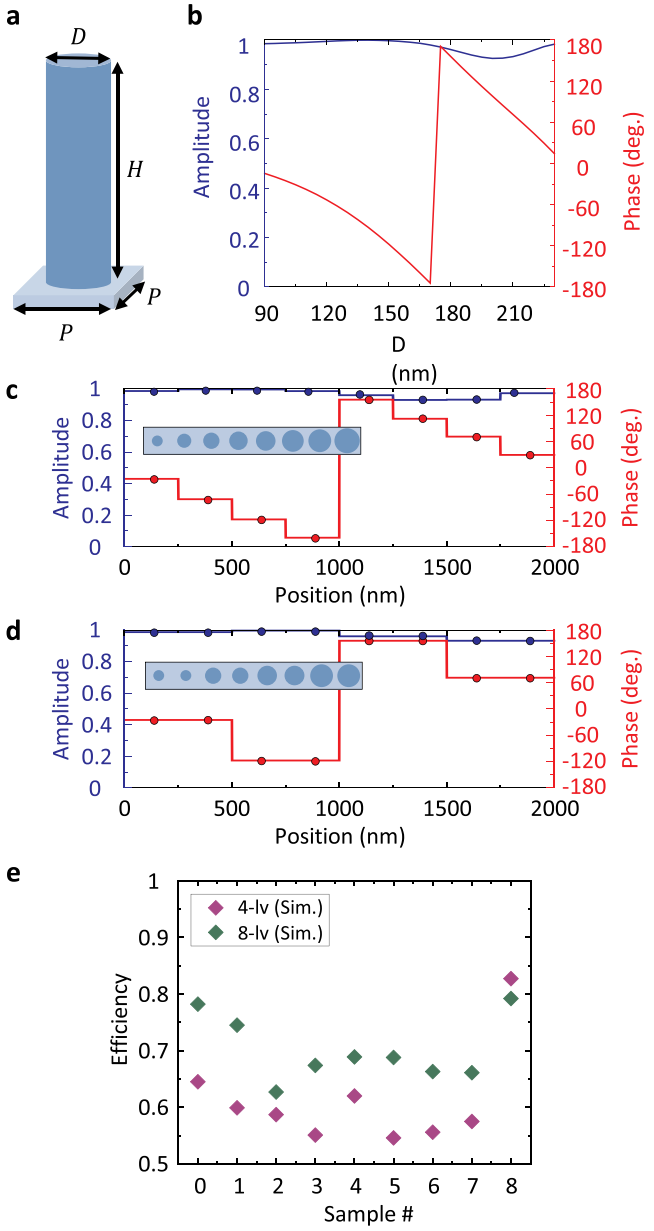

Figure 8. Another example of beam steering devices made of dielectric meta-atoms in transmission. (a) Schematic of the dielectric meta-atom: a TiO_2 cylinder (varying diameter D and fixed height H = 600 nm) supported by a glass substrate with the periodicity P = 250 nm. (b) Corresponding amplitude and phase shift in transmission as a function of D at λ = 632 nm. (c) Eight-level unit cell with dielectric meta-atoms of diameters D = 100, 130, 150, 165, 180, 195, 210, and 225 nm and (d) four-level unit cell with meta-atoms of diameters D = 100, 150, 180, and 210 nm (each element being repeated once). The discrete elements used for the full-wave simulations are shown in the insets of panels (c, d). (e) Metasurface performance as a function of the sample number for eight-level and four-level metasurfaces computed using full-wave simulations.

the phase associated with the substrate, one can decide which element is going to be the most sensitive one.

A metasurface is relatively immune to the meta-atom placement within the unit cell. On the other hand, size variations can rapidly affect the overall efficiency. These findings hold both for eight-level and four-level metasurfaces and for both types of devices; we notice that the steering angle is not influenced by such defects θ.

Measurements on misfabricated metallic metasurfaces, both eight-level and four-level, fully support these findings, which indicate that one can design a metasurface with less stringent considerations than anticipated. This work paves the way for revisiting the design of metasurfaces afresh, beyond the constraints of a periodic perfect lattice, possibly with the help of a deep learning approach.[56]

METHODS

Nanofabrication. Supporting Information, Figure S1 shows the process flow for nanofabrication. A Silicon wafer (100/P/SS/01-100, Center of MicroNanoTechnology at EPFL) was first baked on a hot plate (fabricant) for 5 min at a temperature of 180 °C to dehydrate it (humidity appears detrimental to nanofabrication[57,58]). Then, 1 nm Ti as the adhesion layer followed by 150 nm Au as the mirror, 1 nm Ti and 40 nm SiO2 as the dielectric space, 1 nm Ti, 30 nm gold as the meta-atoms, and finally, 20 nm Cr as the sacrificial layer were deposited using an evaporator (Leybold Optics LAB600H). A negative tone electron-beam photoresist hydrogen silsesquioxane (HSQ, XR-1541-006 DuPont) was then spun-coated on top at 6000 rpm. After electron-beam exposure (Vistec EBPG5000 system, 100 keV and 100 pA) and development (Tetramethylammonium Hydroxide 25%, Honeywell), ion beam etching (Veeco Nexus IBE350, 300 V and 500 mA collimated Ar ion beam) is used to reveal the meta-atoms while maintaining the SiO_2 substrate. The sample is finished by etching the sacrificial Cr layer (TechniEtch Cr01, Microchemicals GmbH) to remove the remaining HSQ and cleaned in isopropanol alcohol and deionized water.

Quasi-Analytical Model. A simple quasi-analytical model is implemented to calculate the momentum provided by the metasurface. For a normal incident plane wave propagating in $-z$-direction, the phase gradient metasurface provides a momentum horizontally in $+x$-direction and the reflected light is redirected into the angle θ as described by the generalized Snell's law.[59] The simplified one-dimension model considers each unit cell as a point light source with its own amplitude and phase: $E(x) = E_x e^{i\phi_x}$. This information after the Fourier transform can be converted into the momentum k_x parallel to the surface. Once the unit cells' periodicity and the superlattice period are determined, we apply Fourier transforms to convert the complex amplitude from direct space into spatial frequencies

$$\tilde{E}(k_x) = \frac{1}{2\pi}\int_{-\infty}^{+\infty} E(x)e^{-ik_x x}\mathrm{d}x \tag{1.1}$$

where $\tilde{E}(k_x)$ is the Fourier transform of the electric field $E(x)$ and $\exp(-ik_x x)$ the phase term associated with the metasurface. The efficiency in the Fourier plane is normalized to the maximum intensity for a perfect mirror, such that the performance of the device can be quantized. A Matlab code implementing this simple model is available in the open dataset (Section 1) associated with this article.

Full-Wave Simulations. The full-wave simulations are performed with COMSOL version 5.6. Periodic boundary conditions are applied in x- and y-directions at the edges of the superlattice. The system is illuminated at normal incidence with a plane wave polarized in the y-direction (λ = 980 nm). The following references are used for the refractive index of gold,[60] silicon,[61] titanium dioxide,[62] and silicon dioxide.[63]

https://doi.org/10.1021/acsphotonics.2c00563
ACS Photonics 2022, 9, 2438−2447

Perfect match layers are applied on both ends. The energy in the different diffraction orders can be obtained directly from COMSOL or extracted from the electric and magnetic fields above the surface at 2 and 2.5 μm using the post-processing provided in the open dataset (Section 2) associated with this article.[64]

Optical Characterization. Supporting Information, Figure S4a shows the optical setup used for the optical characterization of the different metasurfaces fabricated. The measurements are conducted with an inverted microscope (Olympus IX-73) and a 50x objective with NA = 0.9, which can collect the light up to 64°. The light source (LP980-SF15, Thorlabs) is a laser diode coupled into an optical fiber. To generate a linearly polarized plane wave, a collimator and a subsequent linear polarizer are placed at the end of the fiber. A lens with focal distance f = 200 mm is used to convert light reflected from the sample into the Fourier plane, thus providing angular information. As indicated in the main text, the light diverted by the metasurface is normalized to that reflected by a silver mirror to determine the metasurface efficiency. On the contrary, the beam steering metasurface is capable of deflecting the incoming light toward an angle, as shown in the Supporting Information, Figure 4b. The efficiency is defined as the total power of the deflected beam divided by the total power of the light reflected by the silver mirror. A Matlab code is provided in the open dataset (Section 3) associated with this article to post-process the experimental data.[64]

■ ASSOCIATED CONTENT

Supporting Information

The Supporting Information is available free of charge at https://pubs.acs.org/doi/10.1021/acsphotonics.2c00563.

> Figure S1, fabrication process as described in the Methods Section. Figures S2 and S3, miss-fabricated eight-level and four-level devices. Figure S4, optical characterization setup. Figure S5, efficiency of an artificial four-level device calculated with the simple model, neglecting the variations of amplitude. Figure S6, total electric field amplitude distribution and the phase profile for four-level dielectric beam steering metasurfaces (PDF)

■ AUTHOR INFORMATION

Corresponding Author

Olivier J. F. Martin − *Nanophotonics and Metrology Laboratory, Swiss Federal Institute of Technology Lausanne (EPFL), 1015 Lausanne, Switzerland;* orcid.org/0000-0002-9574-3119; Email: olivier.martin@epfl.ch

Authors

Hsiang-Chu Wang − *Nanophotonics and Metrology Laboratory, Swiss Federal Institute of Technology Lausanne (EPFL), 1015 Lausanne, Switzerland;* orcid.org/0000-0002-0738-5586

Karim Achouri − *Nanophotonics and Metrology Laboratory, Swiss Federal Institute of Technology Lausanne (EPFL), 1015 Lausanne, Switzerland*

Complete contact information is available at: https://pubs.acs.org/10.1021/acsphotonics.2c00563

Funding

Funding from the Swiss National Science Foundation (projects 200021_162453 and PZ00P2_193221) and from the European Research Council (ERC-2015-AdG-695206) is gratefully acknowledged.

Notes

The authors declare no competing financial interest.

■ REFERENCES

(1) Bomzon, Z.; Kleiner, V.; Hasman, E. Space-variant polarization state manipulation with computer-generated subwavelength metal stripe gratings. *Opt. Commun.* **2001**, *192*, 169−181.

(2) Sievenpiper, D.; Schaffner, J. H.; Song, H. J.; Loo, R. Y.; Tangonan, G. Two-dimensional beam steering using an electrically tunable impedance surface. *IEEE Trans. Antennas Propag.* **2003**, *51*, 2713−2722.

(3) Lim, S.; Caloz, C.; Itoh, T. Metamaterial-based electronically controlled transmission-line structure as a novel leaky-wave antenna with tunable radiation angle and beamwidth. *IEEE Trans. Microwave Theory Tech.* **2004**, *52*, 2678−2690.

(4) Li, A.; Singh, S.; Sievenpiper, D. Metasurfaces and their applications. *Nanophotonics* **2018**, *7*, 989−1011.

(5) Feng, Q.; Pu, M.; Hu, C.; Luo, X. Engineering the dispersion of metamaterial surface for broadband infrared absorption. *Opt. Lett.* **2012**, *37*, 2133−2135.

(6) Pfeiffer, C.; Grbic, A. Cascaded metasurfaces for complete phase and polarization control. *Appl. Phys. Lett.* **2013**, *102*, No. 231116.

(7) Yao, Y.; Shankar, R.; Kats, M. A.; Song, Y.; Kong, J.; Loncar, M.; Capasso, F. Electrically Tunable Metasurface Perfect Absorbers for Ultrathin Mid-Infrared Optical Modulators. *Nano Lett.* **2014**, *14*, 6526−6532.

(8) Fan, K.; Suen, J. Y.; Liu, X.; Padilla, W. J. All-dielectric metasurface absorbers for uncooled terahertz imaging. *Optica* **2017**, *4*, 601−604.

(9) Li, P.; Dolado, I.; Alfaro-Mozaz, F. J.; Casanova, F.; Hueso, L. E.; Liu, S.; Edgar, J. H.; Nikitin, A. Y.; Velez, S.; Hillenbrand, R. Infrared hyperbolic metasurface based on nanostructured van der Waals materials. *Science* **2018**, *359*, 892−896.

(10) He, J.; Dong, T.; Chi, B.; Zhang, Y. Metasurfaces for Terahertz Wavefront Modulation: a Review. *J. Infrared, Millimeter, Terahertz Waves* **2020**, *41*, 607−631.

(11) Wang, Z.; Wu, Y.; Qi, D.; Yu, W.; Zheng, H. Progress in the design, nanofabrication, and performance of metalenses. *J. Opt.* **2021**, *24*, No. 033001.

(12) Yu, N.; Capasso, F. Flat optics with designer metasurfaces. *Nat. Mater.* **2014**, *13*, 139−150.

(13) Huang, L.; Zhang, S.; Zentgraf, T. Metasurface holography: from fundamentals to applications. *Nanophotonics* **2018**, *7*, 1169−1190.

(14) Sun, S.; He, Q.; Hao, J.; Xiao, S.; Zhou, L. Electromagnetic metasurfaces: physics and applications. *Adv. Opt. Photonics* **2019**, *11*, 380−479.

(15) Chen, W. T.; Zhu, A. Y.; Capasso, F. Flat optics with dispersion-engineered metasurfaces. *Nat. Rev. Mater.* **2020**, *5*, 604−620.

(16) Kamali, S. M.; Arbabi, E.; Arbabi, A.; Faraon, A. A review of dielectric optical metasurfaces for wavefront control. *Nanophotonics* **2018**, *7*, 1041−1068.

(17) Achouri, K.; Bernasconi, G. D.; Butet, J.; Martin, O. J. F. Homogenization and Scattering Analysis of Second-Harmonic Generation in Nonlinear Metasurfaces. *IEEE Trans. Antennas Propag.* **2018**, *66*, 6061−6075.

(18) Shaltout, A. M.; Lagoudakis, K. G.; van de Groep, J.; Kim, S. J.; Vučković, J.; Shalaev, V. M.; Brongersma, M. L. Spatiotemporal light control with frequency-gradient metasurfaces. *Science* **2019**, *365*, 374−377.

(19) Hsiao, H.-H.; Chu, C. H.; Tsai, D. P. Fundamentals and Applications of Metasurfaces. *Small Methods* **2017**, *1*, No. 1600064.

(20) Yoon, G.; Tanaka, T.; Zentgraf, T.; Rho, J. Recent progress on metasurfaces: applications and fabrication. *J. Phys. D: Appl. Phys.* **2021**, *54*, No. 383002.
(21) Baracu, A. M.; Avram, M. A.; Breazu, C.; Bunea, M.-C.; Socol, M.; Stanculescu, A.; Matei, E.; Thrane, P. C. V.; Dirdal, C. A.; Dinescu, A.; Rasoga, O. Silicon Metalens Fabrication from Electron Beam to UV-Nanoimprint Lithography. *Nanomaterials* **2021**, *11*, 2329.
(22) Roberts, A. S.; Pors, A.; Albrektsen, O.; Bozhevolnyi, S. I. Subwavelength Plasmonic Color Printing Protected for Ambient Use. *Nano Lett.* **2014**, *14*, 783−787.
(23) Chu, C. H.; Tseng, M. L.; Chen, J.; Wu, P. C.; Chen, Y.-H.; Wang, H.-C.; Chen, T.-Y.; Hsieh, W. T.; Wu, H. J.; Sun, G.; Tsai, D. P. Active dielectric metasurface based on phase-change medium. *Laser Photonics Rev.* **2016**, *10*, 986−994.
(24) Yan, C.; Yang, K.-Y.; Martin, O. J. F. Fano-resonance-assisted metasurface for color routing. *Light: Sci. Appl.* **2017**, *6*, No. e17017.
(25) Yang, K.-Y.; Verre, R.; Butet, J.; Yan, C.; Antosiewicz, T. J.; Käll, M.; Martin, O. J. F. Wavevector-Selective Nonlinear Plasmonic Metasurfaces. *Nano Lett.* **2017**, *17*, 5258−5263.
(26) Wang, H.; Wang, X.; Yan, C.; Zhao, H.; Zhang, J.; Santschi, C.; Martin, O. J. F. Full Color Generation Using Silver Tandem Nanodisks. *ACS Nano* **2017**, *11*, 4419−4427.
(27) Wu, P. C.; Tsai, W.-Y.; Chen, W. T.; Huang, Y.-W.; Chen, T.-Y.; Chen, J.-W.; Liao, C. Y.; Chu, C. H.; Sun, G.; Tsai, D. P. Versatile Polarization Generation with an Aluminum Plasmonic Metasurface. *Nano Lett.* **2017**, *17*, 445−452.
(28) Ding, F.; Deshpande, R.; Bozhevolnyi, S. I. Bifunctional gap-plasmon metasurfaces for visible light: polarization-controlled unidirectional surface plasmon excitation and beam steering at normal incidence. *Light: Sci. Appl.* **2018**, *7*, 17178.
(29) Wang, H.-C.; Chu, C. H.; Wu, P. C.; Hsiao, H.-H.; Wu, H. J.; Chen, J.-W.; Lee, W. H.; Lai, Y.-C.; Huang, Y.-W.; Tseng, M. L.; Chang, S.-W.; Tsai, D. P. Ultrathin Planar Cavity Metasurfaces. *Small* **2018**, *14*, No. 1703920.
(30) Ray, D.; Raziman, T. V.; Santschi, C.; Etezadi, D.; Altug, H.; Martin, O. J. F. Hybrid Metal-Dielectric Metasurfaces for Refractive Index Sensing. *Nano Lett.* **2020**, *20*, 8752−8759.
(31) Hu, T.; Tseng, C.-K.; Fu, Y. H.; Xu, Z.; Dong, Y.; Wang, S.; Lai, K. H.; Bliznetsov, V.; Zhu, S.; Lin, Q.; Gu, Y. Demonstration of color display metasurfaces via immersion lithography on a 12-inch silicon wafer. *Opt. Express* **2018**, *26*, 19548−19554.
(32) Li, N.; Fu, Y. H.; Dong, Y.; Hu, T.; Xu, Z.; Zhong, Q.; Li, D.; Lai, K. H.; Zhu, S.; Lin, Q.; Gu, Y.; Singh, N. Large-area pixelated metasurface beam deflector on a 12-inch glass wafer for random point generation. *Nanophotonics* **2019**, *8*, 1855−1861.
(33) Dong, Y.; Xu, Z.; Li, N.; Tong, J.; Fu, Y.; Zhou, Y.; Hu, T.; Zhong, Q.; Bliznetsov, V.; Zhu, S.; Lin, Q.; Zhang, D. H.; Gu, Y.; Singh, N. Si metasurface half-wave plates demonstrated on a 12-inch CMOS platform. *Nanophotonics* **2019**, *9*, 149−157.
(34) Dirdal, C. A.; Jensen, G. U.; Angelskar, H.; Thrane, P. C. V.; Gjessing, J.; Ordnung, D. A. Towards high-throughput large-area metalens fabrication using UV-nanoimprint lithography and Bosch deep reactive ion etching. *Opt. Express* **2020**, *28*, 15542−15561.
(35) Cencillo-Abad, P.; Ou, J.-Y.; Plum, E.; Valente, J.; Zheludev, N. I. Random access actuation of nanowire grid metamaterial. *Nanotechnology* **2016**, *27*, No. 485206.
(36) Liu, Z.; Du, H.; Li, Z.-Y.; Fang, N. X.; Li, J. Invited Article: Nano-kirigami metasurfaces by focused-ion-beam induced close-loop transformation. *APL Photonics* **2018**, *3*, No. 100803.
(37) Semple, M.; Hryciw, A. C.; Li, P.; Flaim, E.; Iyer, A. K. Patterning of Complex, Nanometer-Scale Features in Wide-Area Gold Nanoplasmonic Structures Using Helium Focused Ion Beam Milling. *ACS Appl. Mater. Interfaces* **2021**, *13*, 43209−43220.
(38) West, P. R.; Stewart, J. L.; Kildishev, A. V.; Shalaev, V. M.; Shkunov, V. V.; Strohkendl, F.; Zakharenkov, Y. A.; Dodds, R. K.; Byren, R. All-dielectric subwavelength metasurface focusing lens. *Opt. Express* **2014**, *22*, 26212−26221.
(39) Sain, B.; Meier, C.; Zentgraf, T. Nonlinear optics in all-dielectric nanoantennas and metasurfaces: a review. *Adv. Photonics* **2019**, *1*, No. 024002.
(40) Radko, I. P.; Volkov, V. S.; Beermann, J.; Evlyukhin, A. B.; Søndergaard, T.; Boltasseva, A.; Bozhevolnyi, S. I. Plasmonic metasurfaces for waveguiding and field enhancement. *Laser Photonics Rev.* **2009**, *3*, 575−590.
(41) Genevet, P.; Capasso, F.; Aieta, F.; Khorasaninejad, M.; Devlin, R. Recent advances in planar optics: from plasmonic to dielectric metasurfaces. *Optica* **2017**, *4*, 139−152.
(42) Kottmann, J. P.; Martin, O. J. F.; Smith, D. R.; Schultz, S. Non-regularly shaped plasmon resonant nanoparticle as localized light source for near-field microscopy. *J. Microsc.* **2001**, *202*, 60−65.
(43) Abasahl, B.; Santschi, C.; Raziman, T. V.; Martin, O. J. F. Fabrication of plasmonic structures with well-controlled nanometric features: a comparison between lift-off and ion beam etching. *Nanotechnology* **2021**, *32*, No. 475202.
(44) Okazaki, S. High resolution optical lithography or high throughput electron beam lithography: The technical struggle from the micro to the nano-fabrication evolution. *Microelectron. Eng.* **2015**, *133*, 23−35.
(45) Aouani, H.; Wenger, J.; Gerard, D.; Rigneault, H.; Devaux, E.; Ebbesen, T. W.; Mahdavi, F.; Xu, T.; Blair, S. Crucial Role of the Adhesion Layer on the Plasmonic Fluorescence Enhancement. *ACS Nano* **2009**, *3*, 2043−2048.
(46) Jiao, X.; Goeckeritz, J.; Blair, S.; Oldham, M. Localization of Near-Field Resonances in Bowtie Antennae: Influence of Adhesion Layers. *Plasmonics* **2009**, *4*, 37−50.
(47) Siegfried, T.; Ekinci, Y.; Martin, O. J. F.; Sigg, H. Engineering Metal Adhesion Layers That Do Not Deteriorate Plasmon Resonances. *ACS Nano* **2013**, *7*, 2751−2757.
(48) Ekinci, Y.; Christ, A.; Agio, M.; Martin, O. J. F.; Solak, H. H.; Löffler, J. F. Electric and magnetic resonances in arrays of coupled gold nanoparticle in-tandem pairs. *Opt. Express* **2008**, *16*, 13287−13295.
(49) Lévêque, G.; Martin, O. J. F. Optical interactions in a plasmonic particle coupled to a metallic film. *Opt. Express* **2006**, *14*, 9971−9981.
(50) Pors, A.; Bozhevolnyi, S. I. Plasmonic metasurfaces for efficient phase control in reflection. *Opt. Express* **2013**, *21*, 27438−27451.
(51) Ding, F.; Yang, Y.; Deshpande, R. A.; Bozhevolnyi, S. I. A review of gap-surface plasmon metasurfaces: fundamentals and applications. *Nanophotonics* **2018**, *7*, 1129−1156.
(52) Kildishev, A. V.; Boltasseva, A.; Shalaev, V. M. Planar Photonics with Metasurfaces. *Science* **2013**, *339*, No. 1232009.
(53) Ding, F.; Pors, A.; Bozhevolnyi, S. I. Gradient metasurfaces: a review of fundamentals and applications. *Rep. Prog. Phys.* **2018**, *81*, No. 026401.
(54) Achouri, K.; Caloz, C. Design, concepts, and applications of electromagnetic metasurfaces. *Nanophotonics* **2018**, *7*, 1095−1116.
(55) Yan, C.; Raziman, T. V.; Martin, O. J. F. Phase Bifurcation and Zero Reflection in Planar Plasmonic Metasurfaces. *ACS Photonics* **2017**, *4*, 852−860.
(56) Blanchard-Dionne, A.-P.; Martin, O. J. F. Successive training of a generative adversarial network for the design of an optical cloak. *OSA Continuum* **2021**, *4*, 87−95.
(57) Thyagarajan, K.; Santschi, C.; Langlet, P.; Martin, O. J. F. Highly Improved Fabrication of Ag and Al Nanostructures for UV and Nonlinear Plasmonics. *Adv. Opt. Mater.* **2016**, *4*, 871−876.
(58) Wang, X.; Santschi, C.; Martin, O. J. F. Strong Improvement of Long-Term Chemical and Thermal Stability of Plasmonic Silver Nanoantennas and Films. *Small* **2017**, *13*, No. 1700044.
(59) Quaranta, G.; Basset, G.; Martin, O. J. F.; Gallinet, B. Recent Advances in Resonant Waveguide Gratings. *Laser Photonics Rev.* **2018**, *12*, No. 1800017.
(60) Johnson, P. B.; Christy, R. W. Optical Constants of the Noble Metals. *Phys. Rev. B* **1972**, *6*, 4370−4379.
(61) Aspnes, D. E.; Studna, A. A. Dielectric functions and optical parameters of Si, Ge, GaP, GaAs, GaSb, InP, InAs, and InSb from 1.5 to 6.0 eV. *Phys. Rev. B* **1983**, *27*, 985−1009.

https://doi.org/10.1021/acsphotonics.2c00563
ACS Photonics 2022, 9, 2438−2447

(62) Sarkar, S.; Gupta, V.; Kumar, M.; Schubert, J.; Probst, P. T.; Joseph, J.; König, T. A. F. Hybridized guided-mode resonances via colloidal plasmonic self-assembled grating. *ACS Appl. Mater. Interfaces* **2019**, *11*, 13752−13760.
(63) Rodríguez-de Marcos, L. V.; Larruquert, J. I.; Méndez, J. A.; Aznárez, J. A. Self-consistent optical constants of SiO2 and Ta2O5 films. *Opt. Mater. Express* **2016**, *6*, 3622−3637.
(64) Wang, H.-C.; Achouri, K.; Martin, O. J. F. Data set for the manuscript 'Robustness Analysis of Metasurfaces: Perfect Structures are not always the Best' (2.0) [Data set]. https://zenodo.org/record/6606461#.YpihfyhByUk (accessed Jun 02, 2022).

https://doi.org/10.1021/acsphotonics.2c00563
ACS Photonics 2022, 9, 2438−2447